Liu, W. and Chen, Q. 2018. "Development of adaptive coarse grid generation methods for fast fluid dynamics in simulating indoor air flow," *Journal of Building Performance Simulation*, 11(4): 470-484.

To appear in the *Journal of Building Performance Simulation*
Vol. 00, No. 00, Month 20XX, 1–18

Development of adaptive coarse grid generation methods for fast fluid dynamics in simulating indoor airflow

Wei Liu[a,b] and Qingyan Chen[b,c*]

[a]*Zhejiang University-University of Illinois at Urbana-Champaign Institute, International Campus, Zhejiang University, Haining 314400, China;* [b]*Center for High Performance Buildings, School of Mechanical Engineering, Purdue University, West Lafayette, IN 47907, USA;* [c]*Tianjin Key Laboratory of Indoor Air Environmental Quality Control, School of Environmental Science and Engineering, Tianjin University, Tianjin 300072, China*

(*Received 00 Month 20XX; final version received 00 Month 20XX*)

The control of indoor air quality and thermal comfort requires faster-than-real-time simulations of air distribution. One approach to achieve such simulations is to use coarse grid. This study developed two adaptive coarse grid generation methods by analyzing the grid-related truncation errors in the solution of the Navier-Stokes equations by fast fluid dynamics (FFD). Method 1 generates a grid that is coarser than that for a grid-independent solution but can still provide accurate FFD predictions. Method 2 generates a very coarse grid that provides acceptable FFD predictions. This study assessed the performance of the developed methods by using them to simulate three typical indoor airflows. The assessment showed that the coarse grid generated by Method 1 accelerated the FFD simulation by at least two to five times, with similar computational accuracy. The coarse grid generated by Method 2 provided faster-than-real-time FFD simulations for the cases tested in this study.

Keywords: Fast fluid dynamics; Coarse grid; Indoor airflow

1. Introduction

The creation of indoor environments with acceptable air quality and thermal comfort and low energy consumption requires the proper design and control of air distributions in buildings (Chen 2009). This is because indoor air distributions, such as the distributions of chemical species concentrations (CO_2, volatile organic compounds (VOC), etc.) in the air, are related to indoor air quality, and the distributions of air temperature, relative humidity, and air velocity are related to thermal comfort and energy consumption (Standard 2004). A useful tool for predicting the air distributions in buildings is computational fluid dynamics (CFD) (Nielsen 2015). For example, Mahyuddin, Awbi, and Essah (2015) applied CFD simulation to study the airflow in a chamber with respiring manikin. Cropper et al. (2010) coupled CFD with a multi-segmented model of human to investigate the human-environment interaction. Besides, the CFD simulation was also widely applied for the outdoor environment such as wind-driven rain on building facades, etc. (Blocken et al. 2011; Kubilay, Carmeliet, and Derome 2017). Air distribution predicted by CFD simulations can provide a wealth of accurate information about indoor air quality and thermal comfort level in a room or a building even before the building is constructed. However, the computing speed of CFD simulations is far too slow for use in real-time control of HVAC (heating, ventilation, and air-conditioning) systems, where faster-than-real-time simulations of air distribution are required.

*Corresponding author. Email: yanchen@purdue.edu

Efforts to achieve faster-than-real-time simulations of air distributions in indoor environments have included parallel computing that uses multiple CPU (central processing unit) cores (Cohen and Molemaker 2009) or GPUs (graphics processing units) (Zuo and Chen 2010); the development of intermediate models such as coupled CFD and multi-zone models (Gao 2002), coupled zonal model and flow models (Norrefeldt, Grün, and van Treeck 2012; Mucha et al. 2013), and fast fluid dynamics (FFD) (Zuo and Chen 2009); and the utilization of coarse grids (Andrews IV, Loezos, and Sundaresan 2005; VanGilder and Zhang 2008; Wang and Zhai 2012; Jin, Liu, and Chen 2015). These efforts can be integrated in order to increase the computing speed. For example, Zuo and Chen (2010) implemented FFD on a GPU for simulating laminar indoor airflow, and the computing speed was accelerated by 10 to 30 times. Tian, Sevilla, and Zuo (2017) coupled FFD with a cross-platform parallel computing framework OpenCL to accelerate indoor air flow simulations. With the development of hardware, parallel computing can always accelerate the computing speed significantly. In addition, Liu et al. (2016) integrated FFD with a turbulence model, which significantly improved the accuracy of FFD for predicting both transient and steady-state turbulent indoor airflow. As to the use of a coarse grid, Jin, Liu, and Chen (2015) developed an FFD method that used such a grid, but their study focused on modeling the heat source when the grid was coarse. It has not been known whether FFD with a coarse grid could provide predictions that are similar to a grid-independent solution. As a result, at the current stage it is still not practical to integrate FFD, a coarse grid, and parallel computing.

However, there are coarse grid generation methods for CFD simulations that might also be applicable to FFD simulations. A simple approach is the trial-and-error process, which entails the generation of grids with different resolutions and the compares the corresponding solutions to the grid-independent solution in order to identify the desired coarse grid (Wang and Zhai 2012). The trial-and-error process is easy to use, but time-consuming. The most common method is adaptive grid generation by gradients, in which greater numbers of grid cells are used in regions with larger velocity gradients in order to capture the flow features (Zhang et al. 2010), or by an error indicator that indicates the domain with error in the solution (Toosi and Larsson 2017). The primary grid-introduced errors are the truncation errors that arise when the Navier-Stoke equations are discretized (Ham, Lien, and Strong 2002; Tu, Yeoh, and Liu 2012). Toosi and Larsson (2017) developed a new error indicator based on the small-scale energy in a directional manner for grid adaption in large eddy simulations of wall-bounded and free shear flows. With a proper error indicator developed, an adaptive coarse grid generation methods for FFD could thus be established accordingly.

Therefore, this study developed two systematic, algorithm-driven, and anisotropic adaptive coarse grid generation methods by using the error indicator of truncation errors in the solution of the Navier-Stokes equations by FFD. The FFD simulations with the resulting coarse grids were assessed for their ability to predict forced convection flow, mixed convection flow, and natural convection flow in indoor environments in order to evaluate the accuracy of the two methods.

2. Method

According to common practice, all CFD/FFD solutions should be independent of the computational grid in order to avoid two grid-related errors: round-off error and truncation error (Fidkowski and Darmofal 2011; Duan et al. 2015). On one hand, a finer grid leads to larger numerical error due to round-off error. On the other hand, a coarser grid results in larger numerical error due to truncation error. Since our investigation aimed at a coarse grid, this study focused on the grid-related truncation error to develop the error indicator.

This section will first briefly introduce the use of the standard incremental pressure-correction (SIPC) scheme (Goda 1979) with FFD to solve the Navier-Stokes equations. Liu et al. (2016) introduced multiple FFD models and found that the SIPC scheme had slightly better performance than the other schemes in predicting the indoor airflow. Next, this section will address the analysis

of grid-related truncation errors in the solving procedure to develop the error indicator. Finally, we will outline the development of the two adaptive coarse grid generation methods for FFD.

2.1. *Fast fluid dynamics*

For an indoor environment, FFD solves the Navier-Stokes equations for incompressible Newtonian fluid:

$$\frac{\partial U_i}{\partial x_i} = 0 \tag{1}$$

$$\frac{\partial U_i}{\partial t} + U_j \frac{\partial U_i}{\partial x_j} + \frac{1}{\rho}\frac{\partial p}{\partial x_i} - \nu \frac{\partial^2 U_i}{\partial x_j \partial x_j} - \frac{1}{\rho} F_i = 0 \tag{2}$$

where $i, j = 1, 2, 3$; x_i, x_j are the spatial coordinates; U_i is the i_{th} component of the velocity vector; t the time; p the pressure, ρ the density; F_i the i_{th} component of the body forces; and ν the effective viscosity.The SIPC scheme in FFD applies a two-step time-advancement scheme (Ferziger and Peric 2012) that splits the momentum equation (Eq. 2) into two discretized equations:

$$\frac{U_i^* - U_i^n}{\Delta t} = -\frac{1}{\rho}\frac{\partial p^n}{\partial x_i} - U_j^n \frac{\partial U_i^*}{\partial x_j} + \nu \frac{\partial^2 U_i^*}{\partial x_j \partial x_j} + \frac{1}{\rho} F_i \tag{3}$$

$$\frac{U_i^{n+1} - U_i^*}{\Delta t} = -\frac{1}{\rho}\frac{\partial (p^{n+1} - p^n)}{\partial x_i} \tag{4}$$

where U_i^n and U_i^{n+1} represent the air velocity at the previous and current time steps, respectively; U_i^* is the intermediate air velocity; and p^n and p^{n+1} represent the air pressure at the previous and current time steps, respectively.The SIPC scheme resolves the coupled pressure and velocity by the pressure projection method (Chorin 1968), which substitutes Eq. 4 into Eq. 1 to produce

$$\frac{\partial^2 (p^{n+1} - p^n)}{\partial x_i \partial x_i} = \frac{\rho}{\Delta t}\frac{\partial U_i^*}{\partial x_i} \tag{5}$$

The SIPC scheme solves Eq. 3 and the Poisson equation, Eq. 5, in sequence to obtain intermediate velocity U_i^* and the pressure p^{n+1}, respectively. The SIPC scheme then calculates the air velocity at the next time step U_i^{n+1} by using Eq. 4 as follows:

$$U_i^{n+1} = U_i^* - \frac{\Delta t}{\rho}\frac{\partial (p^{n+1} - p^n)}{\partial x_i} \tag{6}$$

This study adopted the re-normalization group (RNG) $k-\varepsilon$ model (Yakhot and Orszag 1986) to simulate the turbulence because the study by Zhang et al. (2007) shows that this model performs well in predicting indoor airflow with different flow features. For the near-wall treatment, this study used the high Reynolds number treatment. Therefore, this study maintained the $y^+ > 30$ and applied the standard wall function.

2.2. *Grid-related truncation error*

In solving Eqs. 3 and 5, the discretization of the temporal term, advection term, and Laplacian terms uses the first-order implicit Euler scheme, the semi-implicit scheme, and the implicit scheme,

respectively. For the temporal term, this study had already applied the first-order implicit Euler scheme in Eq. 3. The Taylor series is used to express the air velocity in the previous time step as

$$U_i^n = U_i^* - \Delta t \frac{\partial U_i^*}{\partial t} + \frac{\Delta t^2}{2}\frac{\partial^2 U_i^*}{\partial t^2} + O(\Delta t^3) \tag{7}$$

This yields

$$\frac{\partial U_i^*}{\partial t} = \frac{U_i^* - U_i^n}{\Delta t} + \frac{\Delta t}{2}\frac{\partial^2 U_i^*}{\partial t^2} + O(\Delta t^2) \tag{8}$$

It is clear that the discretization of the temporal term would introduce only a temporal truncation error. The larger the time step size is, the more significant the introduced numerical error would be. Furthermore, if the flow changed dramatically over time, the second-order derivative of the air velocity over time would be large, and the numerical error would also be significant.

For the advection term, if the first-order upwind scheme is used, the grid-related truncation error for Eq. 3 is $\sum_{j=1}^{3}(|U_j^*|\Delta x_j/2)\partial^2 U_i^*/\partial x_j^2$ (Wang and Zhai 2012).For the diffusion term in Eq. 3, this study used the control volume for one-dimensional airflow, as shown in Fig. 1, as an example to illustrate the numerical error. By using a central difference scheme, we obtain

$$\begin{aligned}
\frac{\partial^2 U_i^*}{\partial x_j \partial x_j} &= \frac{\partial^2 U_1^*}{\partial x_1^2} \\
&= \frac{\left(\frac{\partial U_1^*}{\partial x_1}\right)_e - \left(\frac{\partial U_1^*}{\partial x_1}\right)_w}{\Delta x} \\
&= \frac{\frac{U_1^*(E)-U_1^*(P)}{\Delta x_1} - \frac{U_1^*(P)-U_1^*(W)}{\Delta x_1}}{\Delta x_1} \\
&= \frac{U_1^*(E) - 2U_1^*(P) + U_1^*(W)}{\Delta x_1^2}
\end{aligned} \tag{9}$$

A Taylor series is used to express the parameter on adjacent cells:

$$\begin{aligned}
U_1^*(E) = U_1^*(P) &+ \Delta x_1 \frac{\partial U_1^*}{\partial x_1} + \frac{\Delta x_1^2}{2}\frac{\partial^2 U_1^*}{\partial x_1^2} + \frac{\Delta x_1^3}{6}\frac{\partial^3 U_1^*}{\partial x_1^3} \\
&+ \frac{\Delta x_1^4}{24}\frac{\partial^4 U_1^*}{\partial x_1^4} + \frac{\Delta x_1^5}{120}\frac{\partial^5 U_1^*}{\partial x_1^5} + O(\Delta x_1^6)
\end{aligned} \tag{10}$$

$$\begin{aligned}
U_1^*(W) = U_1^*(P) &- \Delta x_1 \frac{\partial U_1^*}{\partial x_1} + \frac{\Delta x_1^2}{2}\frac{\partial^2 U_1^*}{\partial x_1^2} - \frac{\Delta x_1^3}{6}\frac{\partial^3 U_1^*}{\partial x_1^3} \\
&+ \frac{\Delta x_1^4}{24}\frac{\partial^4 U_1^*}{\partial x_1^4} - \frac{\Delta x_1^5}{120}\frac{\partial^5 U_1^*}{\partial x_1^5} + O(\Delta x_1^6)
\end{aligned} \tag{11}$$

Then the discretized diffusion term can be expressed as:

$$\frac{U_1^*(E) - 2U_1^*(P) + U_1^*(W)}{\Delta x_1^2} = \frac{\partial^2 U_1^*}{\partial x_1^2} + \frac{\Delta x_1^2}{12}\frac{\partial^4 U_1^*}{\partial x_1^4} + O(\Delta x_1^4) \tag{12}$$

The discretization of the diffusion term results in a grid-related truncation error of $O(\Delta x^2)$. Following the same derivation as that for the diffusion term, the discretization of the Laplacian term

in Eq. 5 would result in a grid-related truncation error of $O(\Delta x^2)$.

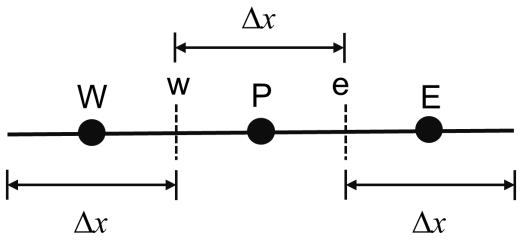

Figure 1. Uniform arrangement of control volume for one-dimensional airflow.

In summary, the discretization of the diffusion term results in a grid-related truncation error of $O(\Delta x^2)$, and that of the convection term results in an error of $O(\Delta x)$ (Wang and Zhai 2012). Therefore, the truncation error introduced by discretizing the convection term is more significant and considered in the generation of a coarse grid for FFD. Since $|U_j^*|\Delta x_j/2$ has the same effect as the physical or turbulent viscosity of the airflow, it is called numerical viscosity. Furthermore, the term $\sum_{j=1}^{3}(|U_j^*|\Delta x_j/2)\partial^2 U_i^*/\partial x_j^2$ is called numerical diffusion. The numerical viscosity is proportional to the grid size, and thus the coarse grid would introduce more significant numerical diffusion and decrease the accuracy.

2.3. *Coarse grid generation methods*

Since the primary grid-related truncation error is the numerical diffusion introduced by discretizing the convection term, this study proposed two adaptive coarse grid generation methods that are based on the analysis of the numerical diffusion in FFD simulations. Method 1 aims to generate a grid that is coarser than that for a grid-independent solution but can still provide accurate FFD predictions. The grid generation procedure is:

(1) Conduct a grid independence test to identify the grid that provides a grid-independent solution. In this step, we recommend the generation of at least $n(n \geq 3)$ uniform grids (acceptable to inexperienced CFD users) with the grid index g_1, $g2$, $\cdots$, g_n, from coarse to fine. Grid g_1 should be very coarse yet still capable of depicting the computational domain. Grid g_k $(2 \leq k \leq n)$ doubles the grid numbers in each direction on the basis of grid g_{k-1}. To identify the grid g_{ind} that provides a grid-independent solution, the predicted air velocity, air temperature, or species concentration by grids g_{k-1} and g_k must be compared with each other quantitatively by using the normalized $RMSE$ Wang and Zhai (2012):

$$RMSE(\phi_1, \phi_2) = \frac{3}{r^P - 1}\sqrt{\frac{\sum_{k=1}^{m}[\phi_1(k) - \phi_2(k)]^2}{\sum_{k=1}^{m}\phi_1(k)^2}} \tag{13}$$

where ϕ_1 and ϕ_2 are the predicted variables with different grid resolutions; m is the number of sampled points; r is the grid refinement factor ($r = 8$ for a three-dimensional case, 4 for a two-dimensional case); and P is the order of the numerical scheme, which is 1 in this study. Wang and Zhai (2012) proposed that if the normalized $RMSE$ is under 10% between a given grid and the next finer grid, the differences between the two predicted results may be considered negligible. The solutions are then considered to be grid independent.

(2) On the basis of FFD prediction with grid g_{ind}, plot the iso-surface for 10% of $Max_{i=1,2,3}(|U_j|\Delta x_j/2)\partial^2 U_i/\partial x_j^2$. A coarse grid is generated by reducing half of the grid in the x_j direction in the domain where the numerical diffusion is smaller than 10% of $Max_{i=1,2,3}(|U_j|\Delta x_j/2)\partial^2 U_i/\partial x_j^2$. The grid index for the coarse grid is c_{11}.

(3) Conduct the FFD simulation with grid c_{11} and evaluate its accuracy by using the normalized $RMSE$ to compare the predicted results with the grid-independent solution.

(4) If the user is satisfied with the accuracy of the FFD prediction using grid c_{11} but requires an even coarser grid, he or she can return to Step 2 but use grid c_{11} instead of grid g_{ind} to generate the coarser grid c_{12}. This procedure can be repeated to obtain the grid c_{1k} that satisfies the users needs.

This method guarantees the accuracy of the FFD simulations with coarse grid $c_{1k}(k \geq 1)$ because a grid-independent solution is always used as a reference. However, the method requires extra effort to obtain the grid-independent solution. When the grid must be used repeatedly and the accuracy of the FFD simulations needs to be ensured in specific applications, such as the inverse design of indoor environments, this method is preferred.

Method 2 emphasizes the ease of coarse grid generation and the computing speed. This method is therefore recommended when the grid is for one-time use and the accuracy of the prediction is not of primary concern. The grid generation procedure is as follows:

(1) A uniform grid, g_1, is generated that is very coarse yet still capable of depicting the computational domain.
(2) On the basis of the FFD simulation with grid g_1, a finer grid, c_{21}, is generated by doubling the grid in the x_j direction in the domain where the numerical diffusion is larger than 10% of $Max_{i=1,2,3}(|U_j|\Delta x_j/2)\partial^2 U_i/\partial x_j^2$.
(3) Step 2 can be repeated to generate an even finer grid, $c_{2k}(k \geq 1)$, as needed.

Grid c_{2k}, obtained by this method, can still be very coarse and is expected to have much higher computing accuracy than grid g_1. Since there is no grid independence test in the second method, the grid generation process is much easier than that in Method 1. However, the accuracy of the FFD simulations with grid c_{2k} cannot be guaranteed.

3. Results

To assess the performance of the two coarse grid generation methods, this study used the methods to conduct FFD simulations for three typical indoor airflow cases: forced convection flow (Wang and Chen 2009), natural convection flow (Betts and Bokhari 2000), and mixed convection flow (Wang and Chen 2009), with experimental data from the literature. The FFD simulations with coarse grids c_{1k} and c_{2k} were compared with grid-independent solutions and the experimental data. The experimental data only includes air velocity and/or air temperature. Since this study did not investigate the wall function or turbulence model, the dimensionless analysis of heat transfer in terms of Nusselt number correlations in typical benchmarks was not involved.

3.1. *Forced convection flow in a simplified room*

The case of forced convection flow in a simplified room was taken from (Wang and Chen 2009). Fig. 2 shows a 2.44 $m \times 2.44$ $m \times 2.44$ m room with a plane jet from the upper left corner. The inlet height was 0.03 m, and the inlet air velocity was 0.455 m/s. The outlet height was 0.08 m. A box in the middle of the room on the floor, with dimensions of 1.22 $m \times 1.22$ $m \times 1.22$ m, was used to simulate furniture. Since the inlet air temperature was the same as that of the room surfaces, this case was isothermal and the airflow type was forced convection.

Following Method 1, this study first conducted a grid independence test by generating four uniform grids (g_1, g_2, g_3, g_4) with different resolutions. The grid numbers were $7,700$, $60,000$, $470,000$, and $3,770,000$, with corresponding grid sizes of 0.12, 0.06, 0.03, and 0.015 m, respectively. We performed FFD simulations with these four grids for 200 s with a time step size of 0.1 s. Fig. 3 compares the grid independence test results for predicted air velocity at four typical locations: positions 1, 3, 5, and 6. As shown in Fig. 2, these locations were in the jet upstream, room center, jet downstream, and a position close to the side wall, respectively. This study also calculated the

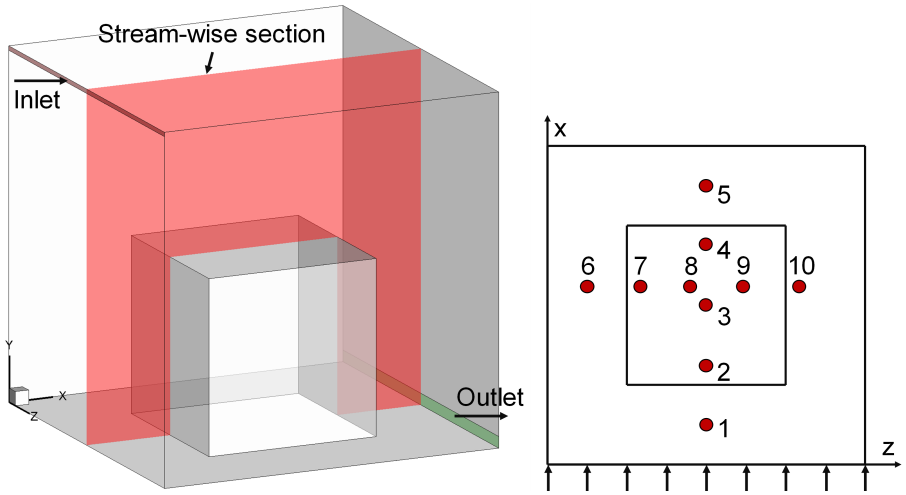

Figure 2. Sketch of the simplified room with a box (left) and the measurement positions (right) (Wang and Chen 2009).

normalized $RMSE$ for air velocity between two grids with different resolutions, as shown in Table 1. The normalized $RMSE$ values for the air velocity between grids g_2 and g_3 were less than 10% at all the locations, which indicated that grid g_2 was the grid g_{ind} that provided a grid-independent solution.

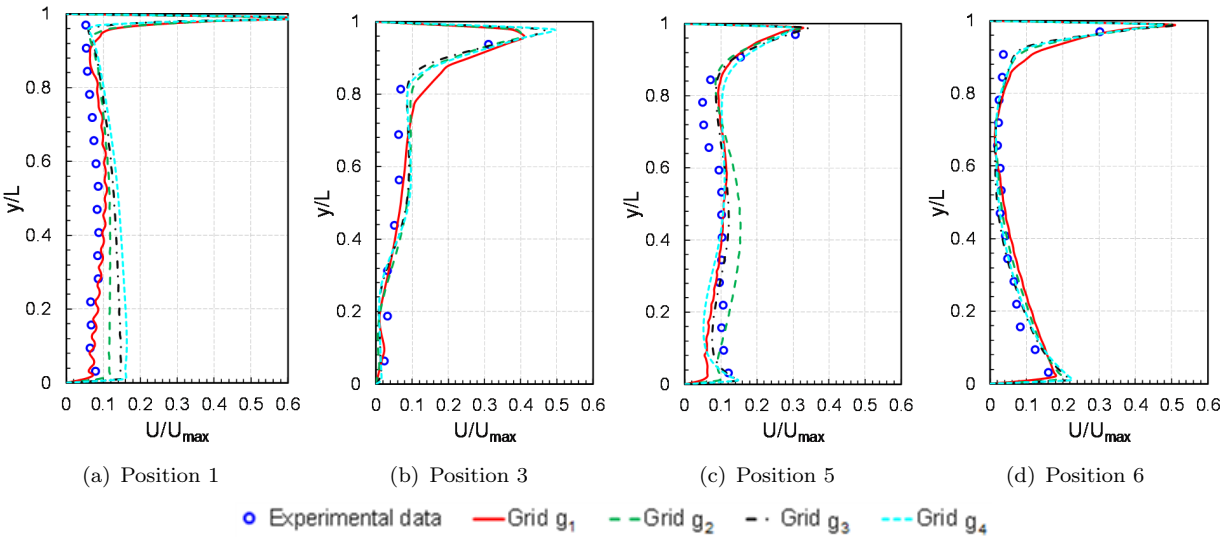

(a) Position 1 (b) Position 3 (c) Position 5 (d) Position 6

Figure 3. Grid independence test for forced convection flow in a simplified room: comparison of air velocity profiles at (a) position 1, (b) position 3, (c) position 5, and (d) position 6.

Table 1. Grid independence tests for forced convection flow in a simplified room: normalized $RMSE$ for air velocity between two grids with Method 1

Coarse grid index	Coarse grid index	Normalized $RMSE$ for air velocity			
		Position 1	Position 3	Position 5	Position 6
g_1	g_2	8.3%	6.6%	11.3%	5.1%
g_2	g_3	7.4%	5.1%	9.7%	4.2%
g_3	g_4	3.6%	3.0%	7.1%	2.2%

Based on the grid-independent solution, Fig. 4(a), 4(b), and 4(c) show the iso-surface for 10% of $Max_{i=1,2,3}(|U_j|\Delta x_j/2)\partial^2 U_i/\partial x_j^2$ in the x_j direction. The numerical diffusion in the regions close to

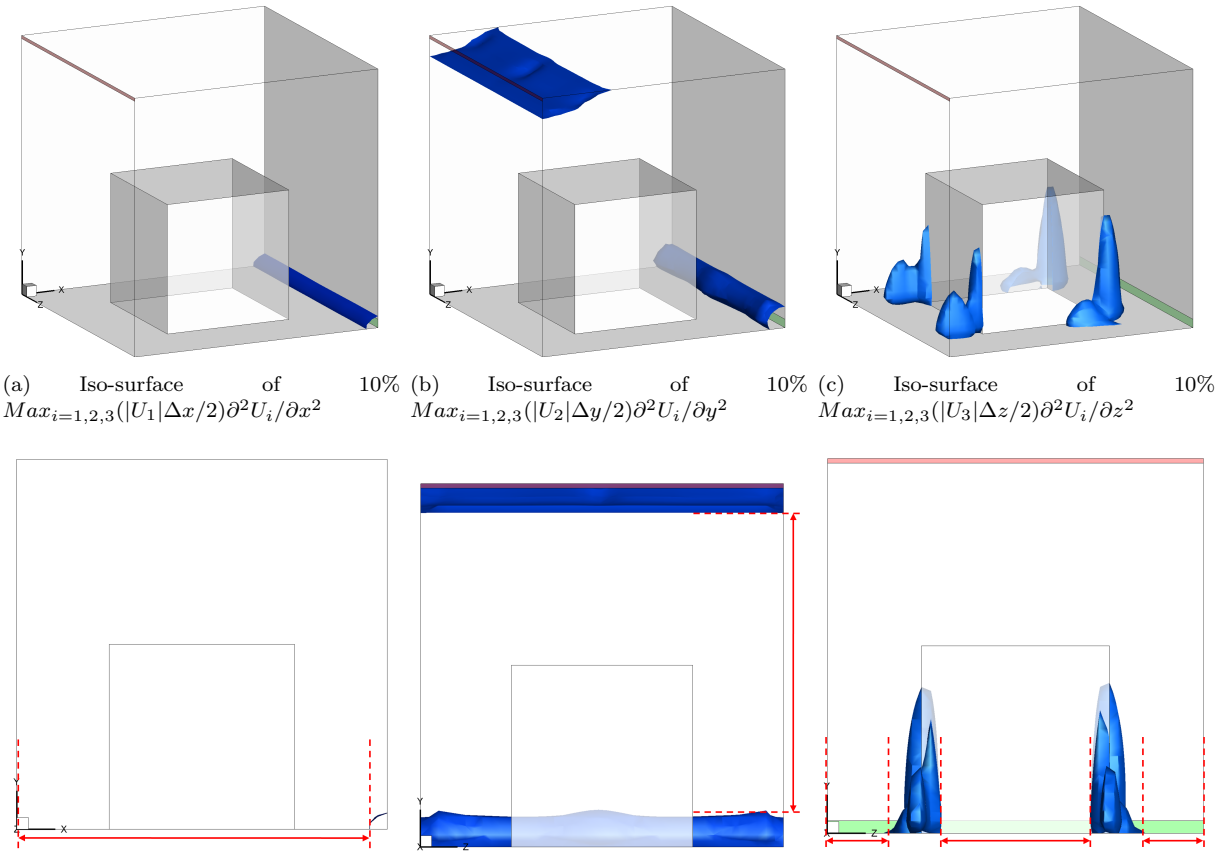

(a) Iso-surface of 10% $Max_{i=1,2,3}(|U_1|\Delta x/2)\partial^2 U_i/\partial x^2$

(b) Iso-surface of 10% $Max_{i=1,2,3}(|U_2|\Delta y/2)\partial^2 U_i/\partial y^2$

(c) Iso-surface of 10% $Max_{i=1,2,3}(|U_3|\Delta z/2)\partial^2 U_i/\partial z^2$

(d) Grid in x direction reduced within the double-arrow region

(e) Grid in y direction reduced within the double-arrow region

(f) Grid in z direction reduced within the double-arrow region

Figure 4. Iso-surface for 10% of $Max_{i=1,2,3}(|U_j|\Delta x_j/2)\partial^2 U_i/\partial x_j^2$ with grid g_{ind} (60,000 cells): (a) in the $x = x_1$ direction, (b) in the $y = x_2$ direction, and (c) in the $z = x_3$ direction; and regions where the grid could be reduced by half: (d) in the x direction, (e) in the y direction, and (f) in the z direction.

the inlet, outlet, and box was significant. The regions where the numerical diffusion was insignificant could then be identified, and the grid there could be reduced by half as shown in Fig. 4(d), 4(e), and 4(f). Finally, this study generated a coarse grid, c_{11}, as shown in Fig. 5(b). As a reference, Fig. 5(a) shows the grid g_{ind} that provided the grid-independent solution. The cell number for grid c_{11} (12,300) was only one fifth of that for grid g_{ind} (60,000). Grid c_{11} was non-uniform and was relatively fine in the regions close to the inlet, outlet, and box.

Next, according to Method 2, this study determined the iso-surface for 10% of $Max_{i=1,2,3}(|U_j|\Delta x_j/2)\partial^2 U_i/\partial x_j^2$ in the x_j direction for the FFD predictions with the coarsest grid, g_1 (7,700 cells), as shown in Fig. 6. We then doubled the grid in the regions where the numerical diffusion was larger than 10% of $Max_{i=1,2,3}(|U_j|\Delta x_j/2)\partial^2 U_i/\partial x_j^2$ in the x_j direction. Fig. 7(b) shows the coarse grid, c_{21}, with 14,900 cells generated by Method 2. The coarsest grid, g_1, is provided in Fig. 7(a) as a reference. Again, grid c_{21} was non-uniform, and the grid was relatively fine in the regions close to the inlet, outlet, and box.

This study evaluated the performance of the two coarse grids, c_{11} and c_{21}, by calculating the normalized $RMSE$ for air velocity as shown in Table 2, where the grid-independent solution with grid g_{ind} is used as a reference. In all the calculations, we set $r = 8$ and $P = 1$ in Eq. 13. Note that because the normalized $RMSE$ values for air velocity were less than 10%, coarse grids c_{11} and c_{21} had very similar performance to that of g_{ind}. This study thus did not further refine the grid by method 2, but generated coarse grid c_{12} (6,372 cells) based on the coarse grid c_{11} by Method 1 (second iteration). The normalized $RMSE$ for air velocity between grids c_{12} and g_{ind} as shown in Table 2 shows that grid c_{12} performed poor and there was no need to further coarsen the grid.

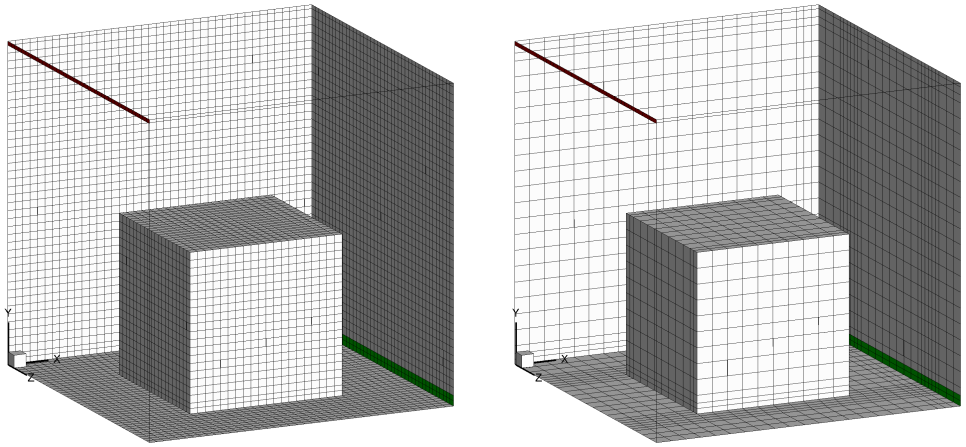

(a) (b)

Figure 5. (a) The grid g_{ind} (60,000 cells) that provided the grid-independent solution and (b) grid c_{11} (12,300 cells) generated by Method 1.

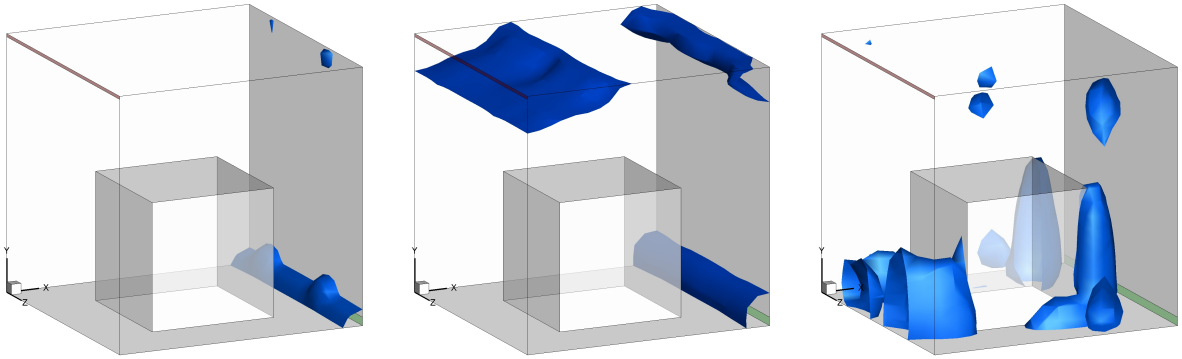

(a) Iso-surface of 10% $Max_{i=1,2,3}(|U_1|\Delta x/2)\partial^2 U_i/\partial x^2$ (b) Iso-surface of 10% $Max_{i=1,2,3}(|U_2|\Delta y/2)\partial^2 U_i/\partial y^2$ (c) Iso-surface of 10% $Max_{i=1,2,3}(|U_3|\Delta z/2)\partial^2 U_i/\partial z^2$

Figure 6. Iso-surface for 10% of $Max_{i=1,2,3}(|U_j|\Delta x_j/2)\partial^2 U_i/\partial x_j^2$ with the coarsest grid g_1 (7,700 grid cells): (a) in the x direction, (b) in the y direction, and (c) in the z direction.

Table 2. Assessing the coarse grid solution for forced convection flow in a simplified room: normalized $RMSE$ for air velocity between two grids

Coarse grid index	Coarse grid index	Normalized $RMSE$ for air velocity				
		Position 1	Position 3	Position 5	Position 6	Average
c_{11}		9.4%	3.1%	4.9%	2.2%	4.9%
c_{12}	g_{ind}	11.5%	18.2%	24.9%	10.0%	16.2%
c_{21}		9.1%	6.3%	7.5%	4.9%	7.0%

Fig. 8 compares the predicted airflow field in the stream-wise section (shown in Fig. 2) with different grid numbers. We found a noticeable difference only in the lower part of the re-circulated region (on the left side of the box). The predictions with the two coarse grid methods were able to capture the major flow features in this simplified room.

3.2. *Natural convection flow in a tall cavity*

The second case that this study used to assess the two methods was that of natural convection flow in a tall cavity from (Betts and Bokhari 2000). Fig. 9 shows the dimensions of the cavity. The cold and hot wall temperatures were 15.1^oC and 34.7^oC, respectively, with a corresponding Rayleigh

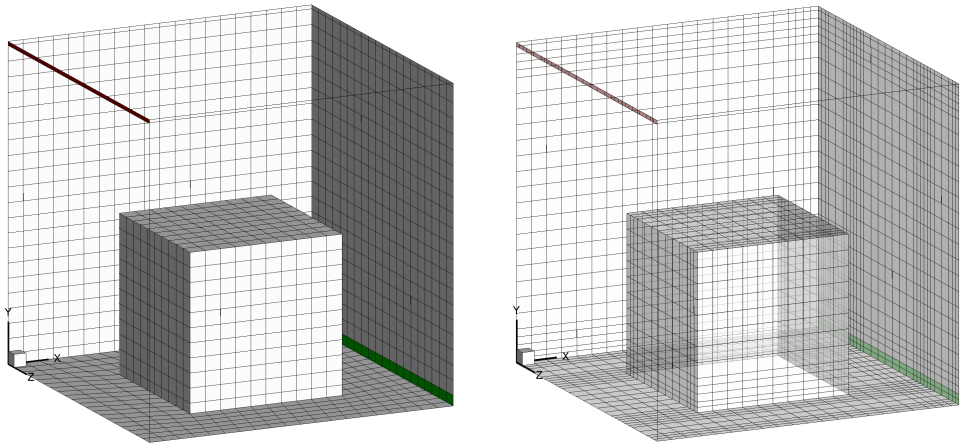

(a) (b)

Figure 7. (a) Coarsest grid g_1 (7,700 cells) and (b) coarse grid c_{21} (14,900 cells) generated by Method 2.

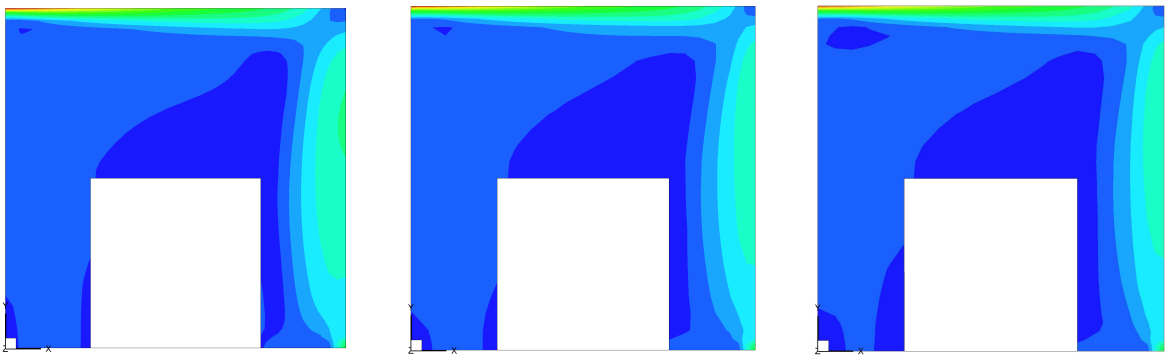

(a) Grid-independent solution (b) Grid c_{11} (c) Grid c_{21}

Figure 8. Predicted flow fields in the stream-wise section with (a) grid g_{ind} (60,000 cells), (b) grid c_{11} (12,300 cells), and (c) grid c_{21} (14,900 cells).

number of 0.86×10^6. Due the temperature difference in this case was large, this study thus considered the density variation by using the ideal gas law, rather than the Boussinesq approximation (Boussinesq 1903). The top and bottom walls were treated as adiabatic. Since the experimental data showed that the airflow was approximately two-dimensional in the vicinity of the center plane, the computational domain used in this study was two-dimensional.

This study tested the two coarse grid generation methods in sequence. A grid independence test was first conducted by generating five uniform grids (g_1, g_2, g_3, g_4, and g_5) with different resolutions. The grid numbers were 680, 2,730, 10,000, 41,000, and 166,000, respectively. We calculated the flow for a physical time of 100 s with a time step size of 0.02 s. The grid independence tests compared the predicted air velocity and temperature profiles at $y/H = 0.3$, 0.5, and 0.7, as shown in Fig. 10. Grid g_4 (41,000 cells) was the grid g_{ind} that provided a grid-independent solution, as confirmed by the normalized $RMSE$ values in Table 3. The air temperature was normalized by the cold and hot wall temperatures before it was used to calculate the corresponding normalized $RMSE$. Note that we calculated the normalized $RMSE$ for both air velocity and temperature and selected the variable with larger errors (air velocity in this case) to determine whether a grid independent solution had been obtained.

On the basis of the grid independence test, this study then plotted the iso-surface for 10% of $Max_{i=1,2}(|U_j|\Delta x_j/2)\partial^2 U_i/\partial x_j^2$ with grid g_{ind} (grid-independent solution) and grid g_1 (the coarsest grid) as shown in Figs. 11 and 12, respectively. Fig. 11 shows that the numerical diffusion in the interior region was smaller than 10% of $Max_{i=1,2}(|U_j|\Delta x_j/2)\partial^2 U_i/\partial x_j^2$ with $g_{ind} = 41,000$ cells, and the grid in this region could be reduced by half by using Method 1, as shown in

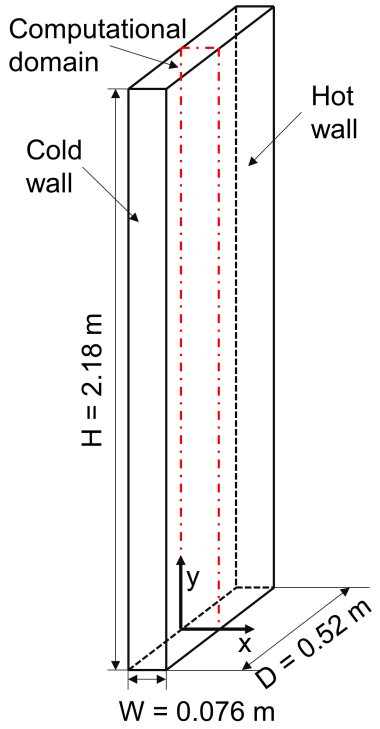

Figure 9. Sketch of the tall cavity Betts and Bokhari (2000) and the computational domain (dash-dot lines).

Table 3. Grid independence test for natural convection flow in a tall cavity: normalized $RMSE$ for air velocity/temperature between two grids for Method 1

Coarse grid index	Coarse grid index	Normalized $RMSE$ for air velocity/temperature $y/H = 0.3$	$y/H = 0.5$	$y/H = 0.7$
g_1	g_2	29.6%/4.8%	56.1%/13.8%	29.7%/4.4%
g_2	g_3	23.0%/3.5%	10.4%/3.2%	23.1%/3.3%
g_3	g_4	11.5%/1.5%	11.4%/1.4%	11.5%/1.5%
g_4	g_5	4.9%/1.5%	4.8%/1.5%	4.9%/1.5%

Fig. 13(a). This study used tetrahedral cells to connect the near-wall fine grid and the interior coarse grid. Fig. 12 depicts the numerical diffusion at the two ends, which was larger than 10% of $Max_{i=1,2}(|U_j|\Delta x_j/2)\partial^2 U_i/\partial x_j^2$ with grid $g_1 = 680$ cells. The grid at the two ends was doubled by using Method 2, as shown in Fig. 13(b). We determined that the cell number of grid c_{11} was $25,000$, while that of grid c_{21} was only 970.

Finally, this study conducted the FFD simulation with coarse grids c_{11} and c_{21}. Table 4 lists the normalized $RMSE$ values for air velocity/temperature between grids c_{11}, c_{21}, and g_1 and grid g_{ind}. In these calculations, we set $r = 4$ and $P = 1$ in Eq. 13. The predictions with grid c_{11} were almost the same as those with g_{ind} at all the positions. This study thus further applied Method 1 to obtain coarse grid c_{12} with $17,600$ cells and its performance was again almost the same with the grid g_{ind} at all the positions. This study did not further coarsen the grid because the larger size difference between fine and coarse grids would lead to poor grid quality. The prediction with grid c_{21} indeed differed from that with g_{ind} at all the positions, but the performance of grid c_{21} was much better than that of grid g_1 (the coarsest grid). This is because the normalized $RMSE$ value for the air velocity and temperature between grids c_{21} and g_{ind} was much smaller than that between grids g_1 and g_{ind}, as shown in Table 4. This study further applied Method 2 and obtained the grid c_{22} with $2,060$ cells. The predictions with grid c_{22} were almost the same as those with g_{ind} at all the positions, this study thus did not further refine the grid by Method 2.

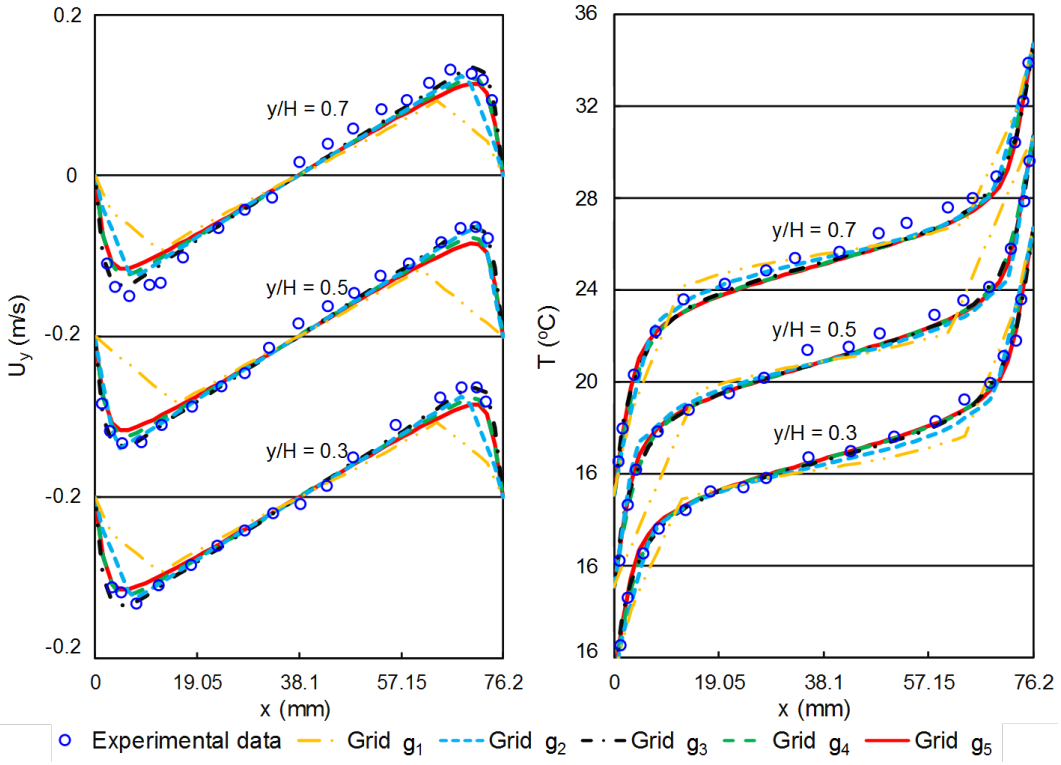

Figure 10. Grid independence test for natural convection flow in a cavity: comparison of air velocity and temperature profiles at $y/H = 0.3$, 0.5, and 0.7.

(a) Iso-surface of $10\%Max_{i=1,2}(|U_1|\Delta x/2)\partial^2 U_i/\partial x^2$

(b) Iso-surface of $10\%Max_{i=1,2}(|U_2|\Delta y/2)\partial^2 U_i/\partial y^2$

Figure 11. Iso-surface for 10% of $Max_{i=1,2}(|U_j|\Delta x_j/2)\partial^2 U_i/\partial x_j^2$ with grid g_{ind} (41,000) in (a) the $x_1 = x$ direction and (b) the $x_2 = y$ direction.

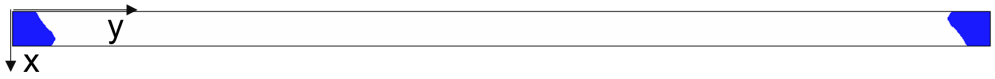

(a) Iso-surface of $10\%Max_{i=1,2}(|U_1|\Delta x/2)\partial^2 U_i/\partial x^2$

(b) Iso-surface of $10\%Max_{i=1,2}(|U_2|\Delta y/2)\partial^2 U_i/\partial y^2$

Figure 12. Iso-surface for 10% of $Max_{i=1,2}(|U_j|\Delta x_j/2)\partial^2 U_i/\partial x_j^2$ with the coarsest grid, g_1 (680 cells) in (a) the $x_1 = x$ direction and (b) the $x_2 = y$ direction.

3.3. *Mixed convection flow in a simplified room*

The third case used in this study to assess the two methods was a mixed convection flow that combined forced convection and natural convection in a simplified room. The case setup was the same as that for the case of forced convection flow in a simplified room in Section 3.1, with the addition of 700 W of heat inside the box shown in Fig. 2. The heated box formed a thermal plume,

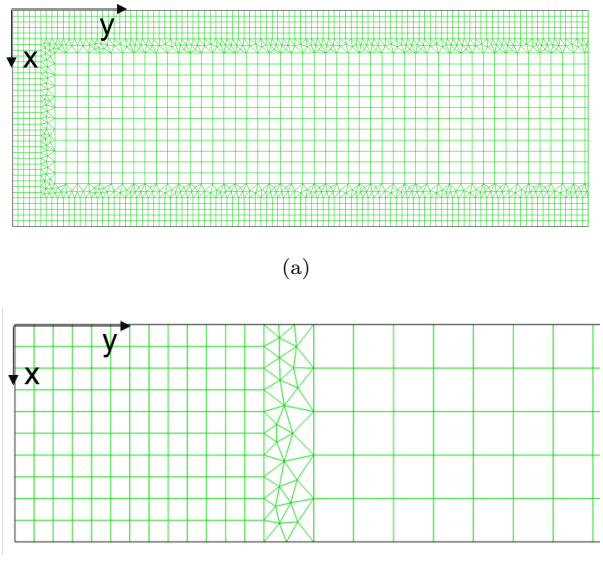

(a)

(b)

Figure 13. Distribution of (a) grid c_{11} (25,000 cells) and (b) grid c_{21} (970 cells).

Table 4. Assessing the coarse grid solution for natural convection flow in a tall cavity: normalized $RMSE$ for air velocity/temperature between two grids

Coarse grid index	Coarse grid index	Normalized $RMSE$ for air velocity/temperature			
		$y/H = 0.3$	$y/H = 0.5$	$y/H = 0.7$	Average
c_{11}	g_{ind}	1.8%/0.2%	1.9%/0.2%	2.2%/0.2%	2.0%/0.2%
c_{12}		6.8%/0.8%	4.5%/0.5%	6.0%/0.5%	5.8%/0.6%
c_{21}		29.6%/4.6%	26.2%/5.2%	29.8%/4.4%	28.5%/4.7%
c_{22}		9.7%/3.1%	8.7%/4.0%	9.8%/2.9%	9.4%/3.3%
g_1		36.7%/6.4%	54.1%/11.1%	36.8%/6.2%	42.5%/7.9%

and the airflow type in the room was mixed convection. The supply air temperature was 22.2^oC. The temperatures of the box surface, ceiling, surrounding walls, and floor were 36.7, 25.8, 27.4, and 26.9^oC, respectively. The Boussinesq approximation (Boussinesq 1903) was applied to simulate the buoyancy effect.

Following a very similar approach to that in the previous cases, grid independence tests were conducted with four uniform grids (g_1, g_2, g_3, and g_4). The grid numbers were 7,700, 60,000, 470,000, and 3,770,000, respectively, which were the same as those in Section 3.1. The numerical setup in the FFD simulations was also the same as that in Section 3.1. Fig. 14 compares the predicted air velocity and temperature at four typical locations: positions 1, 3, 5, and 6 (shown in Fig. 2). Table 5 provides the normalized $RMSE$ for air velocity and temperature between two grids. The normalized $RMSE$ values for air velocity and temperature between grids g_2 and g_3 were smaller than 10% at all the positions. Therefore, grid g_2 (60,000 cells) was the grid g_{ind} that provided a grid-independent solution.

Figs. 15 and 16 plot the iso-surface for 10% of $Max_{i=1,2,3}(|U_j|\Delta x_j/2)\partial^2 U_i/\partial x_j^2$ for grid g_{ind} and the coarsest grid, g_1, respectively. As shown in Fig. 15, we used Method 1 to reduce grid g_{ind} by half in the regions where the numerical diffusion was smaller than 10% of $Max_{i=1,2,3}(|U_j|\Delta x_j/2)\partial^2 U_i/\partial x_j^2$ in the x_j direction, in order to generate coarse grid c_{11}. Next, as shown in Fig. 16, we used Method 2 to double grid g_1 in the regions where the numerical diffusion was larger than 10% of $Max_{i=1,2,3}(|U_j|\Delta x_j/2)\partial^2 U_i/\partial x_j^2$ in the x_j direction, in order to generate grid c_{21}. These coarse grids, c_{11} and c_{21}, are illustrated in Fig. 17. The corresponding cell numbers were 18,300 and 19,000, respectively.

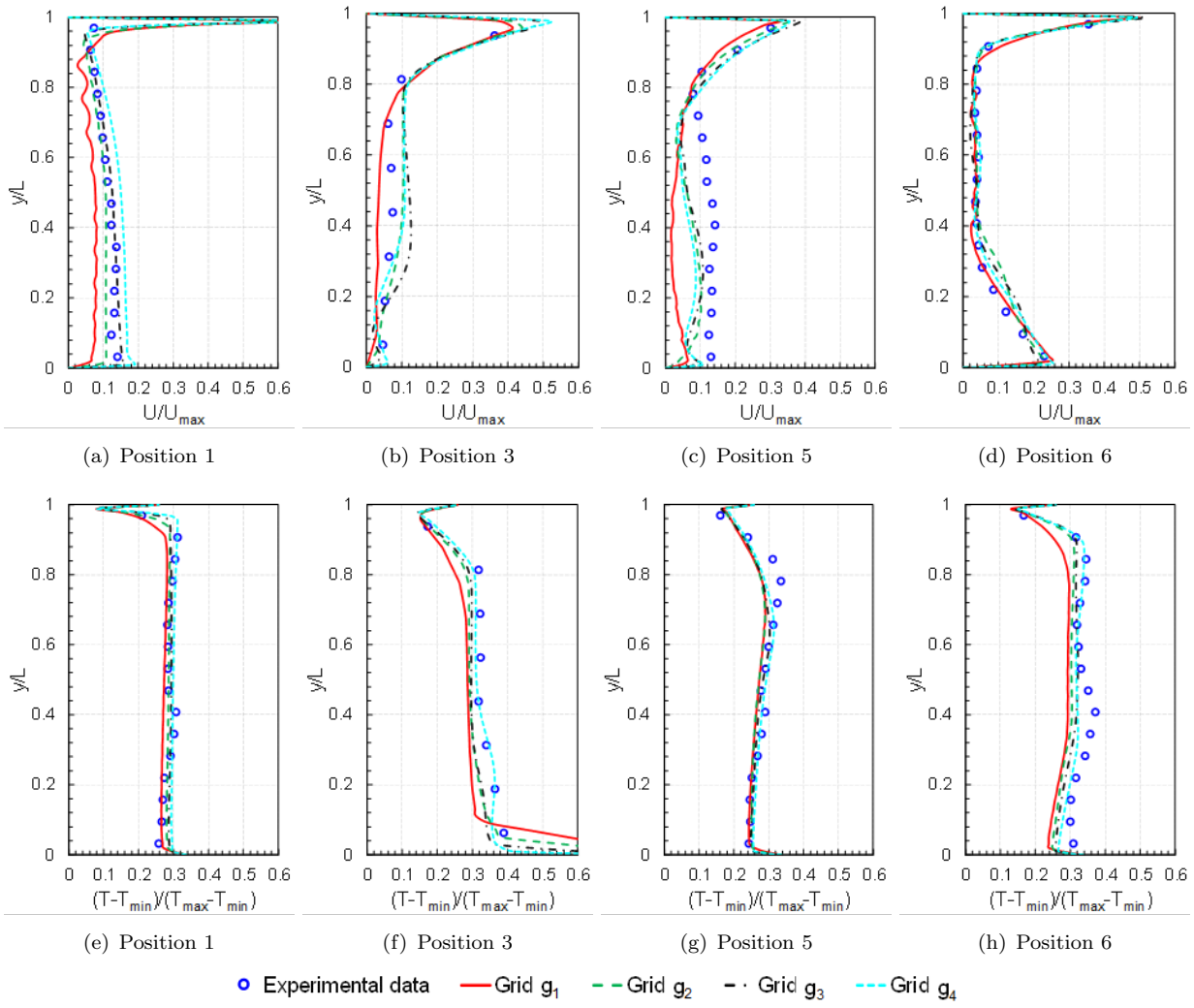

(a) Position 1 (b) Position 3 (c) Position 5 (d) Position 6

(e) Position 1 (f) Position 3 (g) Position 5 (h) Position 6

Figure 14. Grid independence test for mixed convection flow in a simplified room: comparison of air velocity profiles at (a) position 1, (b) position 3, (c) position 5, and (d) position 6; and comparison of air temperature profiles at (e) position 1, (f) position 3, (g) position 5, and (h) position 6.

Table 5. Grid independence test for mixed convection flow in a simplified room: normalized $RMSE$ for air velocity/temperature between two grids for Method 1

Coarse grid index	Coarse grid index	Normalized $RMSE$ for air velocity/temperature			
		Position 1	Position 3	Position 5	Position 6
g_1	g_2	10.6%/2.2%	12.9%/4.9%	17.1%/0.6%	7.5%/2.6%
g_2	g_3	9.5%/1.4%	5.5%/4.7%	6.3%/1.3%	3.9%/1.7%
g_3	g_4	5.9%/1.5%	5.6%/4.6%	4.8%/1.4%	4.6%/1.7%

To assess the performance of the coarse grids, c_{11} and c_{21}, this study conducted FFD simulations with these grids and compared the predictions with the grid-independent solution. According to the normalized $RMSE$ values for air velocity and temperature, shown in Table 6, the coarse grids had very similar performance to that of grid g_{ind}. This study further applied Method 1 to generate grid c_{12} with $4,700$ cells. The performance of grid c_{12} differed from that of the grid g_{ind} as shown in Table 6, this study thus did not further coarsen the grid by Method 1.

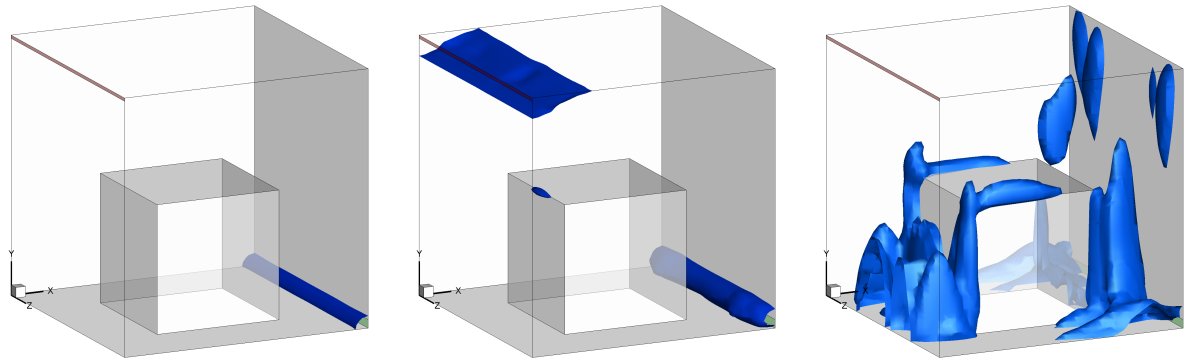

(a) Iso-surface of 10% $Max_{i=1,2,3}(|U_1|\Delta x/2)\partial^2 U_i/\partial x^2$ (b) Iso-surface of 10% $Max_{i=1,2,3}(|U_2|\Delta y/2)\partial^2 U_i/\partial y^2$ (c) Iso-surface of 10% $Max_{i=1,2,3}(|U_3|\Delta z/2)\partial^2 U_i/\partial z^2$

Figure 15. Iso-surface for 10% of $Max_{i=1,2,3}(|U_j|\Delta x_j/2)\partial^2 U_i/\partial x_j^2$ with grid g_{ind} (60,000 cells): (a) in the x direction, (b) in the y direction, and (c) in the z direction.

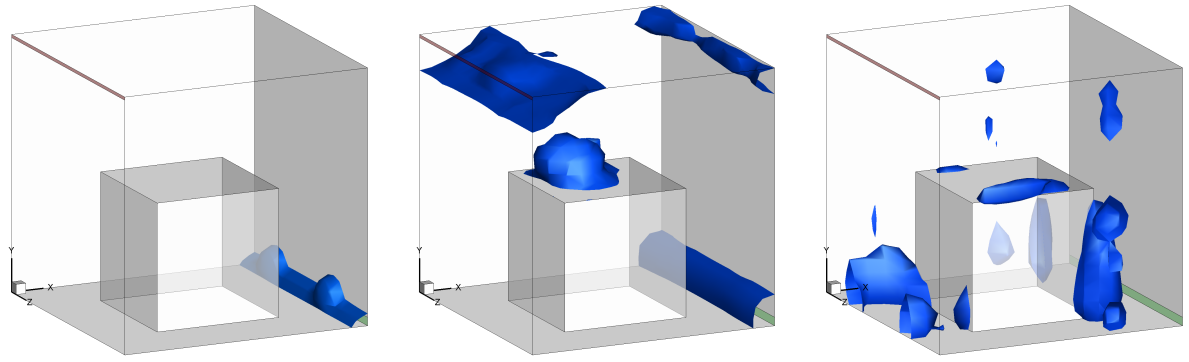

(a) Iso-surface of 10% $Max_{i=1,2,3}(|U_1|\Delta x/2)\partial^2 U_i/\partial x^2$ (b) Iso-surface of 10% $Max_{i=1,2,3}(|U_2|\Delta y/2)\partial^2 U_i/\partial y^2$ (c) Iso-surface of 10% $Max_{i=1,2,3}(|U_3|\Delta z/2)\partial^2 U_i/\partial z^2$

Figure 16. Iso-surface for 10% of $Max_{i=1,2,3}(|U_j|\Delta x_j/2)\partial^2 U_i/\partial x_j^2$ with the coarsest grid, g_1 (7,700 grid cells): (a) in the x direction, (b) in the y direction, and (c) in the z direction.

Table 6. Assessing the coarse grid solution for mixed convection flow in a simplified room: normalized $RMSE$ for air velocity/temperature between two grids

Coarse grid index	Coarse grid index	Normalized $RMSE$ for air velocity/temperature				
		Position 1	Position 3	Position 5	Position 6	Average
c_{11}		3.7%/1.6%	2.4%/2.6%	3.7%/1.0%	7.5%/2.3%	4.3%/1.9%
c_{12}	g_{ind}	9.6%/2.4%	10.4%/2.5%	16.0%/2.1%	8.4%/3.9%	11.1%/2.7%
c_{21}		4.3%/1.1%	5.1%/4.2%	6.6%/0.9%	4.9%/1.3%	5.2%/1.9%

4. Discussions

This study applied the first-order upwind scheme to discretize the convection term. As a result, the primary grid-related truncation error arose from the numerical diffusion. If a higher-order scheme, for example, the Quadratic Upstream Interpolation for Convective Kinematics (QUICK) scheme (Leonard 1979), is used to discretize the convection term, the corresponding grid-related truncation error is $-\sum_{j=1}^{3}(|U_j^*|\Delta x_j^2/24)\partial^3 U_i^*/\partial x_j^3$, which has the same order of accuracy as that for the grid-related truncation error obtained by discretizing the diffusion term. Thus, the latter error cannot be neglected. The total grid-related truncation error is $\sum_{j=1}^{3}[-(|U_j^*|\Delta x_j^2/24)\partial^3 U_i^*/\partial x_j^3 + (\Delta x_j^2/12)\partial^4 U_i^*/\partial x_j^4]$ and should be considered in the coarse grid generation procedure. Besides, this study only considered structured mesh since the geometry of the three cases were simple. For

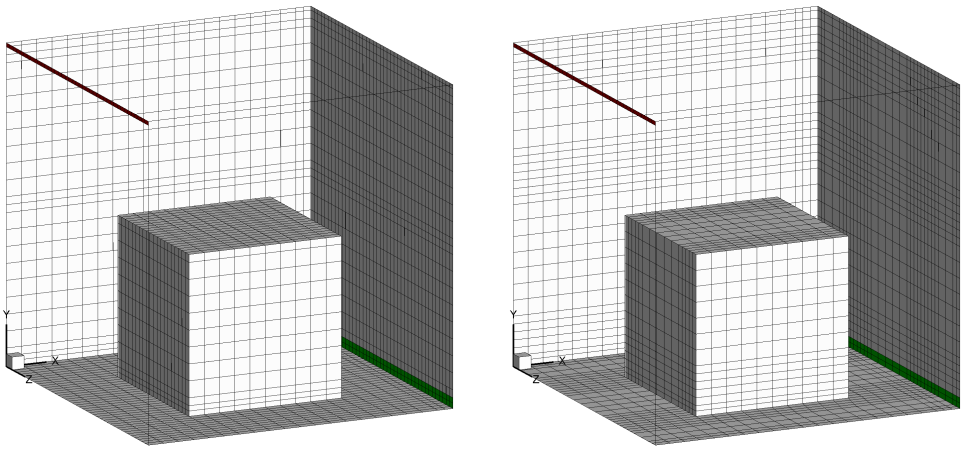

(a) (b)

Figure 17. (a) Grid c_{11} (18,300 cells) generated by Method 1 and (b) grid c_{21} (19,000 cells) generated by Method 2.

complex geometries, the unstructured grid imposes fewer topological restrictions on the user and is easier to use. As long as the numerical error could be determined for the unstructured grid and the corresponding numerical scheme, the algorithm developed in this study could still be applied. This total numerical error is dependent on the numerical scheme and grid type applied in the FFD simulations.

The coarse grid generation methods developed in this investigation were intended to further accelerate the computing speed of FFD. To determine how much faster the FFD simulations would be with coarse grids c_{1k} and c_{2k}, we compared the computing time (t_{comp}) over the physical flow time (t_{phy}) for the grid-independent solutions and the FFD simulations with the two coarse grids, c_{11} and c_{21}, as shown in Table 7. The time used to generate the coarse grid was not taken into consideration. All the calculations were carried out on one core of an Intel Xeon W3565 processor with a frequency of 3.2 GHz. With grid c_{11}, generated by Method 1, the computational speed of the FFD simulations was increased by two to five times. With grid c_{21}, generated by Method 2, it was possible to achieve faster-than-real-time simulations of the three indoor airflow cases investigated in this study.

Table 7. Summary of the computing time (t_{comp}) over the physical flow time (t_{phy}) for the grid-independent solutions and the FFD simulations with the coarse grids

Coarse grid index	t_{comp}/t_{phy}		
	g_{ind}	c_{11}	c_{21}
Forced convection flow	3.07	0.59	0.65
Natural convection flow	9.67	5.20	0.35
Mixed convection flow	3.52	0.93	0.97

5. Conclusions

This study developed two adaptive coarse grid generation methods by analyzing the grid-related truncation errors in the solution of the Navier-Stokes equations by FFD. The two methods start with a uniform grid that is easy or inexperienced users to create. We assessed the performance of the two coarse grid generation methods by applying them to three typical indoor airflows. Our results have led to the following conclusions:

- Method 1 was able to generate a non-uniform coarse grid, and its grid number was only one

fifth to one half of that for the grid that provided the grid-independent solution. Accordingly, the coarse grid generated by Method 1 was able to accelerate the FFD simulation by at least two to five times, and it maintained similar computational accuracy to that of the grid-independent solution.

- Method 2 started with a uniform grid that was very coarse yet still capable of depicting the computational domain, and refined the grid to a non-uniform but still rather coarse grid. The coarse grid generated by Method 2 improved the computational accuracy significantly and provided faster-than-real-time FFD simulation for the cases investigated in this study.
- The two methods developed in this study can generate easy-to-use and effective coarse grids for FFD simulations. Method 1 is recommended when the grid needs to be used repeatedly and when the accuracy of the FFD simulations is essential. Method 2 is recommended when the grid is for one-time use and the accuracy of the prediction is not of primary concern.

Acknowledgement

This research is partially supported by the national key project of the Ministry of Science and Technology, China, on Green Buildings and Building Industrialization through Grant No. 2016YFC0700500, and by the U.S. Department of Homeland Security, Science and Technology Directorate, Office of University Programs, under Grant Award 2013-ST-061-ED0001. The views and conclusions contained in this document are those of the authors and should not be interpreted as necessarily representing the official policies, either expressed or implied, of the U.S. Department of Homeland Security.

References

Andrews IV, Arthur T, Peter N Loezos, and Sankaran Sundaresan. 2005. "Coarse-grid simulation of gas-particle flows in vertical risers." *Industrial & engineering chemistry research* 44 (16): 6022–6037.

Betts, PL, and IH Bokhari. 2000. "Experiments on turbulent natural convection in an enclosed tall cavity." *International Journal of Heat and Fluid Flow* 21 (6): 675–683.

Blocken, Bert, Ted Stathopoulos, Jan Carmeliet, and Jan LM Hensen. 2011. "Application of computational fluid dynamics in building performance simulation for the outdoor environment: an overview." *Journal of Building Performance Simulation* 4 (2): 157–184.

Boussinesq, Joseph. 1903. *Théorie analytique de la chaleur: mise en harmonie avec la thermodynamique et avec la théorie mécanique de la lumière*. Vol. 2. Gauthier-Villars.

Chen, Qingyan. 2009. "Ventilation performance prediction for buildings: A method overview and recent applications." *Building and environment* 44 (4): 848–858.

Chorin, Alexandre Joel. 1968. "Numerical solution of the Navier-Stokes equations." *Mathematics of computation* 22 (104): 745–762.

Cohen, J, and M Jeroen Molemaker. 2009. "A fast double precision CFD code using CUDA." *Parallel Computational Fluid Dynamics: Recent Advances and Future Directions* 414–429.

Cropper, Paul C, Tong Yang, Malcolm Cook, Dusan Fiala, and Rehan Yousaf. 2010. "Coupling a model of human thermoregulation with computational fluid dynamics for predicting human–environment interaction." *Journal of Building Performance Simulation* 3 (3): 233–243.

Duan, Ran, Wei Liu, Luyi Xu, Yan Huang, Xiong Shen, Chao-Hsin Lin, Junjie Liu, Qingyan Chen, and Balasubramanyam Sasanapuri. 2015. "Mesh type and number for the CFD simulations of air distribution in an aircraft cabin." *Numerical Heat Transfer, Part B: Fundamentals* 67 (6): 489–506.

Ferziger, Joel H, and Milovan Peric. 2012. *Computational methods for fluid dynamics*. Springer Science & Business Media.

Fidkowski, Krzysztof J, and David L Darmofal. 2011. "Review of output-based error estimation and mesh adaptation in computational fluid dynamics." *AIAA journal* 49 (4): 673–694.

Gao, Y. 2002. "Coupling of computational fluid dynamics and a multizone airflow analysis program for indoor environmental design." *Cambridge, MA., Massachusetts Institute of Technology* .

Goda, Katuhiko. 1979. "A multistep technique with implicit difference schemes for calculating two-or three-dimensional cavity flows." *Journal of Computational Physics* 30 (1): 76–95.

Ham, FE, FS Lien, and AB Strong. 2002. "A Cartesian grid method with transient anisotropic adaptation." *Journal of Computational Physics* 179 (2): 469–494.

Jin, Mingang, Wei Liu, and Qingyan Chen. 2015. "Simulating buoyancy-driven airflow in buildings by coarse-grid fast fluid dynamics." *Building and Environment* 85: 144–152.

Kubilay, A, J Carmeliet, and D Derome. 2017. "Computational fluid dynamics simulations of wind-driven rain on a mid-rise residential building with various types of facade details." *Journal of Building Performance Simulation* 10 (2): 125–143.

Leonard, Brian P. 1979. "A stable and accurate convective modelling procedure based on quadratic upstream interpolation." *Computer methods in applied mechanics and engineering* 19 (1): 59–98.

Liu, Wei, Ruoyu You, Jie Zhang, and Qingyan Chen. 2016. "Development of a fast fluid dynamics-based adjoint method for the inverse design of indoor environments." *Journal of Building Performance Simulation* 1–18.

Mahyuddin, Norhayati, Hazim B Awbi, and Emmanuel A Essah. 2015. "Computational fluid dynamics modelling of the air movement in an environmental test chamber with a respiring manikin." *Journal of Building Performance Simulation* 8 (5): 359–374.

Mucha, Katharina, Christoph Nytsch-Geusen, Daniel Wölki, and Christoph van Treeck. 2013. "A zonal room model in combined simulation with a physiological human resoinse model to quantify indoor heat stress risks." In *13th International Conference of the International Building Performance (BS 2013),* .

Nielsen, Peter V. 2015. "Fifty years of CFD for room air distribution." *Building and Environment* 91: 78–90.

Norrefeldt, Victor, Gunnar Grün, and Christoph van Treeck. 2012. "Use of the VEPZO model to optimize a hybrid ventilation system." *Berlin, Germany* 26: 28.

Standard, ASHRAE. 2004. "Standard 55-2004Thermal Environmental Conditions for Human Occupancy." *ASHRAE Inc., Atlanta, GA* .

Tian, Wei, Thomas Alonso Sevilla, and Wangda Zuo. 2017. "A systematic evaluation of accelerating indoor airflow simulations using cross-platform parallel computing." *Journal of Building Performance Simulation* 10 (3): 243–255.

Toosi, Siavash, and Johan Larsson. 2017. "Anisotropic grid-adaptation in large eddy simulations of wall-bounded and free shear flows." In *55th AIAA Aerospace Sciences Meeting,* 0978.

Tu, Jiyuan, Guan Heng Yeoh, and Chaoqun Liu. 2012. *Computational fluid dynamics: a practical approach.* Butterworth-Heinemann.

VanGilder, James W, and Xuanhang Simon Zhang. 2008. "Coarse-Grid CFD: The Effect of Grid Size on Data Center Modeling.." *ASHRAE Transactions* 114 (2).

Wang, Haidong, and Zhiqiang Zhai. 2012. "Application of coarse-grid computational fluid dynamics on indoor environment modeling: Optimizing the trade-off between grid resolution and simulation accuracy." *HVAC&R Research* 18 (5): 915–933.

Wang, Miao, and Qingyan Chen. 2009. "Assessment of various turbulence models for transitional flows in an enclosed environment (RP-1271)." *HVAC&R Research* 15 (6): 1099–1119.

Yakhot, Victor, and Steven A Orszag. 1986. "Renormalization-group analysis of turbulence." *Physical review letters* 57 (14): 1722.

Zhang, Rui, Yongjie Zhang, Khee Poh Lam, and David H Archer. 2010. "A prototype mesh generation tool for CFD simulations in architecture domain." *Building and Environment* 45 (10): 2253–2262.

Zhang, Zhao, Wei Zhang, Zhiqiang John Zhai, and Qingyan Yan Chen. 2007. "Evaluation of various turbulence models in predicting airflow and turbulence in enclosed environments by CFD: Part 2Comparison with experimental data from literature." *Hvac&R Research* 13 (6): 871–886.

Zuo, Wangda, and Qingyan Chen. 2009. "Real-time or faster-than-real-time simulation of airflow in buildings." *Indoor Air* 19 (1): 33–44.

Zuo, Wangda, and Qingyan Chen. 2010. "Simulations of air distributions in buildings by FFD on GPU." *HVAC&R Research* 16 (6): 785–798.